Electronic Supplementary Information

Cage-confinement of gas-phase ferrocene in zeolitic imidazolate frameworks to synthesize high-loading and atomically dispersed Fe-N codoped carbon for efficient oxygen reduction reaction

Guanying Ye,[a] *Qian He,*[c] *Suqin Liu,**[ab] *Kuangmin Zhao,*[a] *Yuke Su,*[a] *Weiwei Zhu,*[a] *Rongjiao Huang,*[a] *and Zhen He **[ab]

[a]College of Chemistry and Chemical Engineering, Central South University, Changsha, Hunan 410083, P. R. China.

[b]Hunan Provincial Key Laboratory of Chemical Power Sources, Central South University, Changsha, Hunan 410083, P. R. China.

[c]Cardiff Catalyst Institute, School of Chemistry, Cardiff University, CF103AT Cardiff, United Kingdom

*Corresponding authors.

E-mail addresses: sqliu2003@126.com (S. L.); zhenhe@csu.edu.cn (Z. H.)

This file includes:

Fig. S1 to S12

Table S1 to S5

1. Molecular modeling.

In order to demonstrate the rationality of this cage-confinement synthesis strategy, a supercell (4×4×1) of ZIF-8 was constructed. **Fig.** S1a shows the molecular model of this supercell. By measuring the distance between two atoms both ends of the pore in (002) and (011) crystal planes, the measured distance of the pore of ZIF-8 is about 6 Å, 12 Å and 18 Å. The molecular size of FeCp is about 4 Å, which is suitable to enter the porous structure of ZIF-8, suggesting that it is feasible to realize the adsorption of the vapor-phase FeCp molecules in the ZIF-8 skeleton structure.

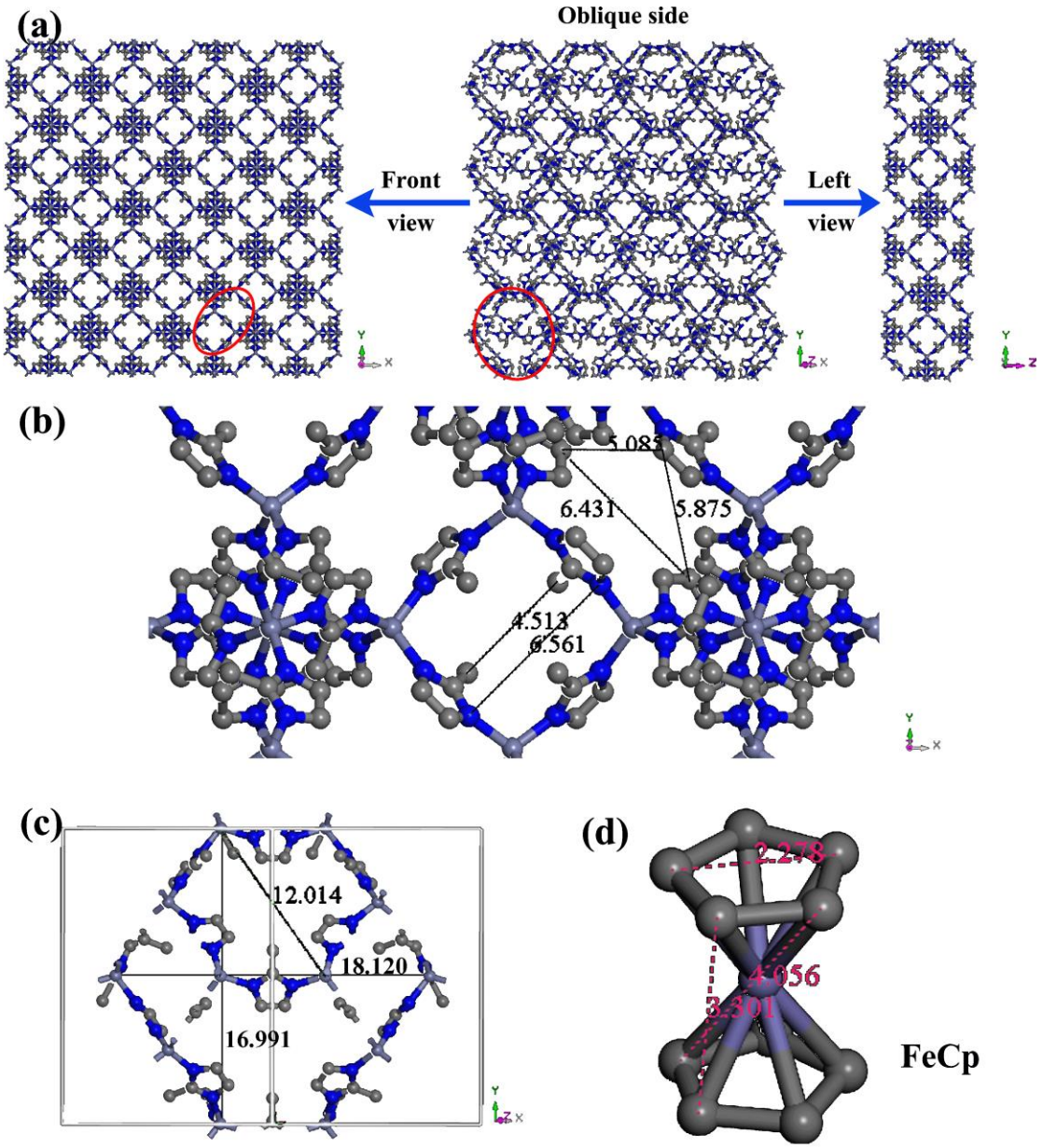

Fig. S1. (a) The molecular model of ZIF-8 supercell. Measurement of ZIF-8 (b) (002) crystal plane and (c) (011) crystal plane. (d) Molecular size of FeCp.

2. HAADF-STEM and EDS mapping analysis of FeCp@ZIF-8.

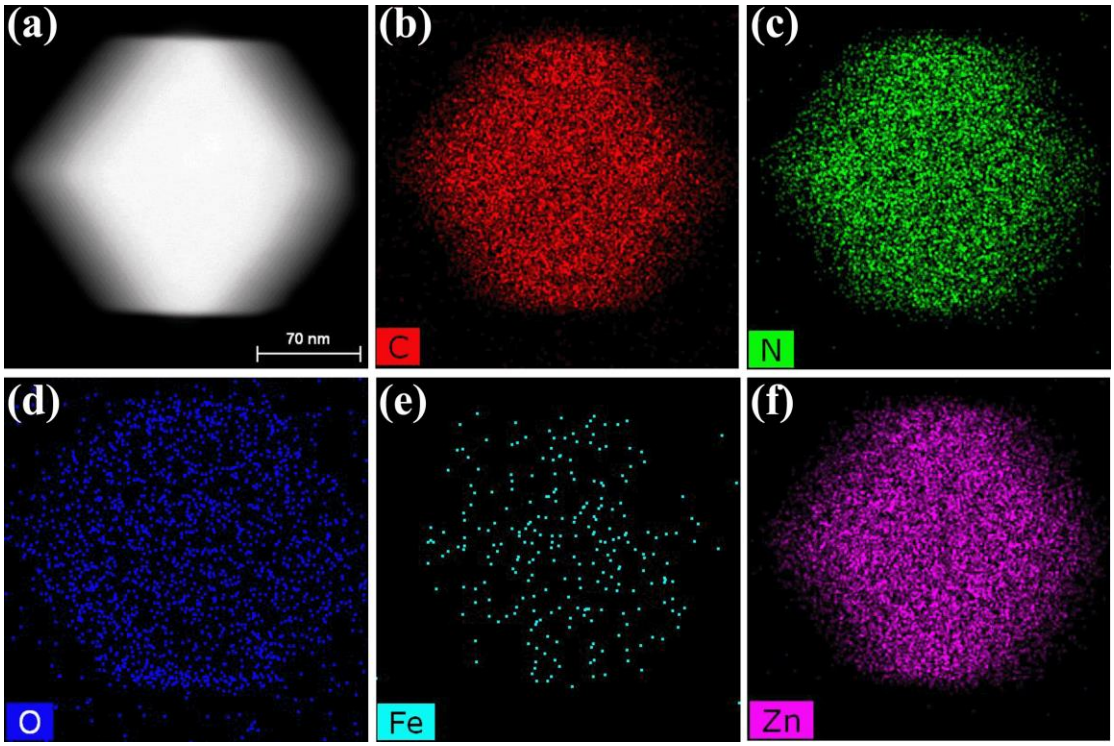

Fig. S2. (a) HAADF-STEM and (b-f) EDS mapping analysis of FeCp@ZIF-8.

3. Simulation of the adsorbed FeCp in the ZIF-8 cage at different adsorption temperatures.

The weight ratios of Fe in the FeCp@ZIF-8 precursors are 0.12, 0.64, 1.20 and 2.46 wt% at the adsorption temperatures of 80, 105, 130 to 155 ℃, respectively. Based on the iron content, the molar ratios of FeCp in the FeCp@ZIF-8 precursors can be calculated. The molar ratios between FeCp and ZIF-8 in the FeCp@ZIF-8 precursors are then calculated to be 1:6, 4:6, 9:6 and 19:6, respectively, as the temperature increase from 80 to 155 ℃, as shown by the simulated molecular structures in **Fig.** S3.

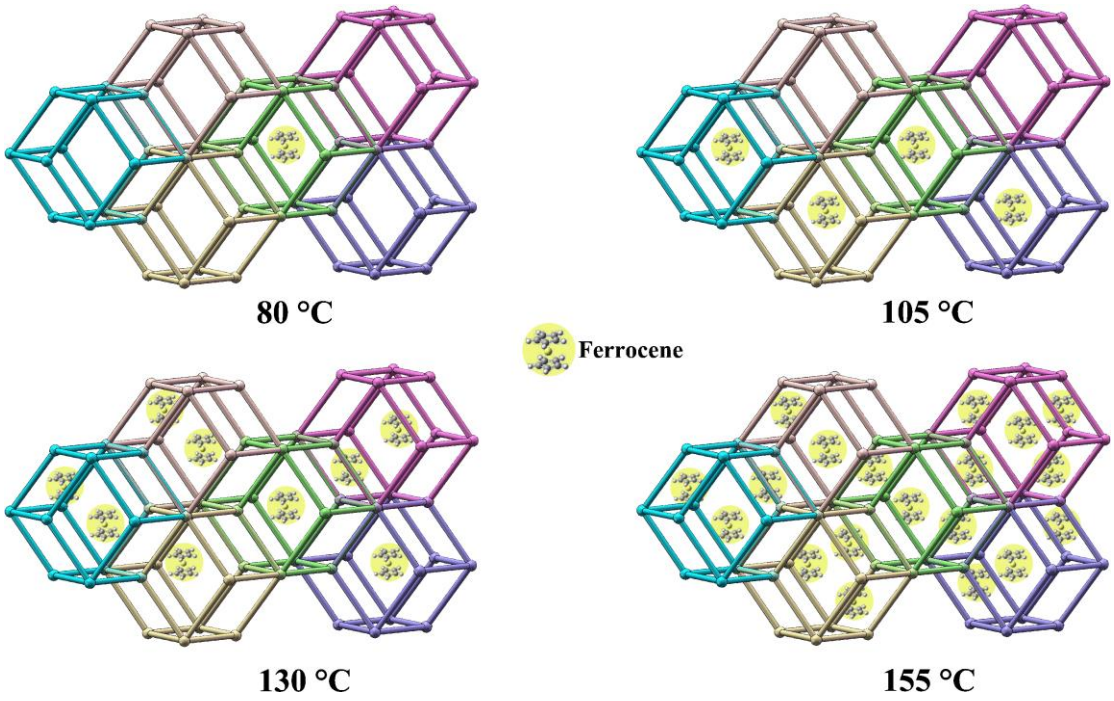

Fig. S3. The simulated models of FeCp@ZIF-8 prepared at different adsorption temperatures.

4. UV-vis characterization of the FeCp@ZIF-8 prepared at 155 ℃ for different adsorption time.

The relative contents of FeCp in the FeCp@ZIF-8 precursors were obtained by measuring the absorbance of the precursors at 250 nm (corresponding to the FeCp absorption) by ultraviolet-visible absorption spectroscopy. 8 mg sample dissolve in 10 mL mixed solution containing with 0.5 M H_2SO_4 and ethanol (v/v, 1/1). With the increase of adsorption time, the UV-vis absorbance of FeCp at the wavelength of 250 nm shows an increasing tendency and reaches an adsorption equilibrium after 9 h, inferring that FeCp content in the FeCp@ZIF-8 increases with the adsorption time.

This result suggests that the content of iron in the FeCp@ZIF-8 precursor could be controlled by adjusting the adsorption time at a given temperature.

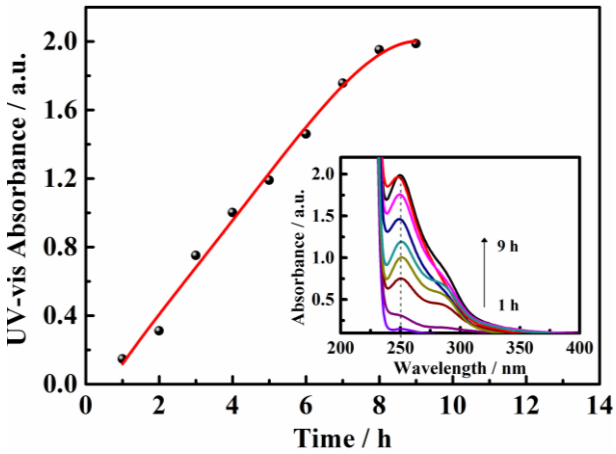

Fig. S4. UV-vis spectras of FeCp@ZIF-8 treated at 155 ℃ for different time.

5. Average particle sizes of the FeCp@ZIF-8 precursor and their corresponding carbonization products.

The particle size distribution of the fabricated ZIF-8, FeCp@ZIF-8, N/C and Fe-N/C-155 was statistically analyzed based on their corresponding SEM images by manually measuring at least 30 particles (for each sample) using the Nano measurement software.

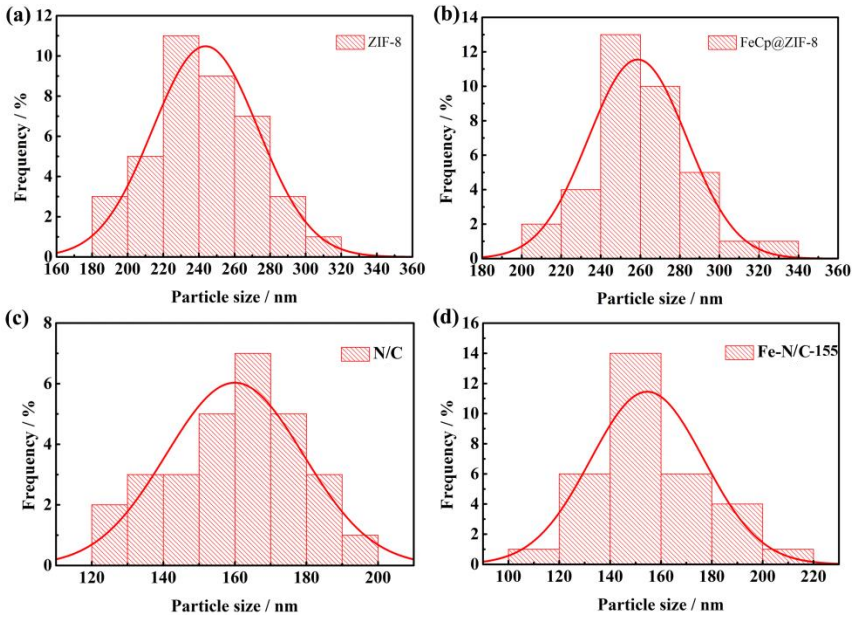

Fig. S5. Particle size distribution of (a) ZIF-8, (b) FeCp@ZIF-8, (c) N/C, and (d) Fe-N/C-155.

6. TEM images of Fe-N/C-155.

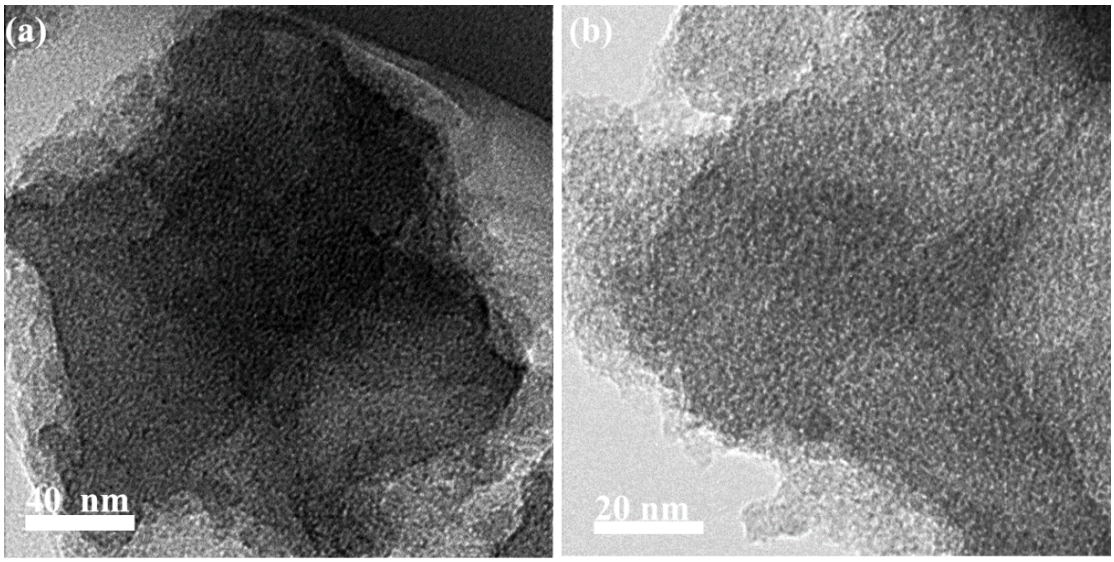

Fig. S6. TEM images of Fe-N/C-155 at different magnifications.

7. XRD patterns of FeCp@ZIF-8 after being pyrolyzed at different temperatures.

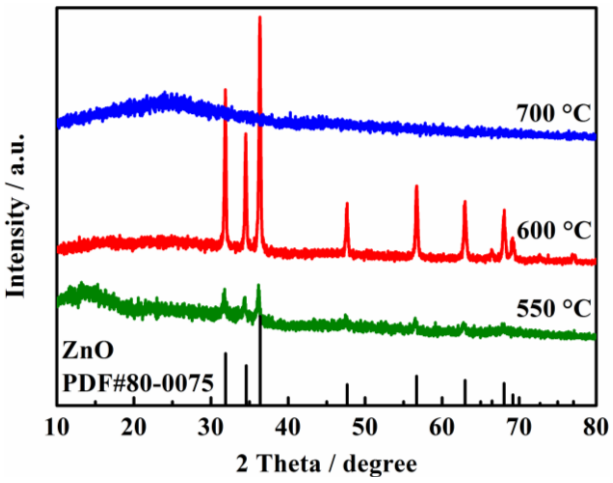

Fig. S7. XRD patterns of FeCp@ZIF-8 after being pyrolyzed at different temperatures under an Ar/H_2 atmosphere.

8. The XPS survey spectrum of N/C and the High-resolution Fe 2p XPS spectra of Fe-N/C.

The signal of surface iron observed by the XPS is about 0.86 at% in Fe-N/C-155. According to the fitting of the Fe 2p spectrum (**Fig.** S8b), the existing valence state of iron in the carbon matrix is Fe(II). Previous research reported that Fe(II) was more active than Fe(III) [1,2]. It can be speculated that Fe(II) formed via the cage-confinement synthesis strategy is more conducive to the formation of the Fe-N_x active site with a higher activity.

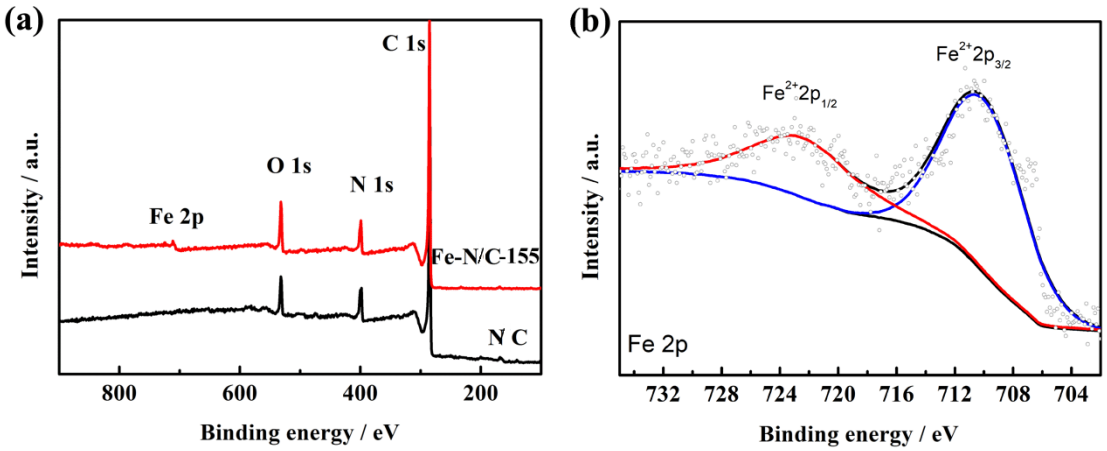

Fig. S8. (a) XPS survey spectra of N/C and Fe-N/C-155. (b) High-resolution Fe 2p XPS spectrum of Fe-N/C-155.

9. The ORR performance of Fe-N/C derived from the FeCp@ZIF-8 precursors synthesized with different adsorption time.

As the simple acid etching can not completely dissolve the iron in the synthesized Fe-N/C catalysts, 10 mg of the Fe-N/C catalyst derived from the FeCp@ZIF-8 precursor synthesized with different adsorption time was calcined in air at 600 ℃ for 2 h to remove all the carbon but remain the metal oxides (e.g., ZnO and FeO_x). Then, the product after the calcination could be completely dissolved in 50 mL of 3 M H_2SO_4 and characterized by UV-vis spectroscopy. With the prolongation of the adsorption time, the iron content is increased (shown by the enhancement of the iron ion absorbance at 305 nm). Meanwhile the catalytic performance of the as-prepared Fe-N/C catalysts also show an increasing trend as the Fe content increases (**Fig.** S9b), inferring that the doping-level of Fe is a key factor affecting the catalytic performance of the synthesized Fe-N/C catalysts.

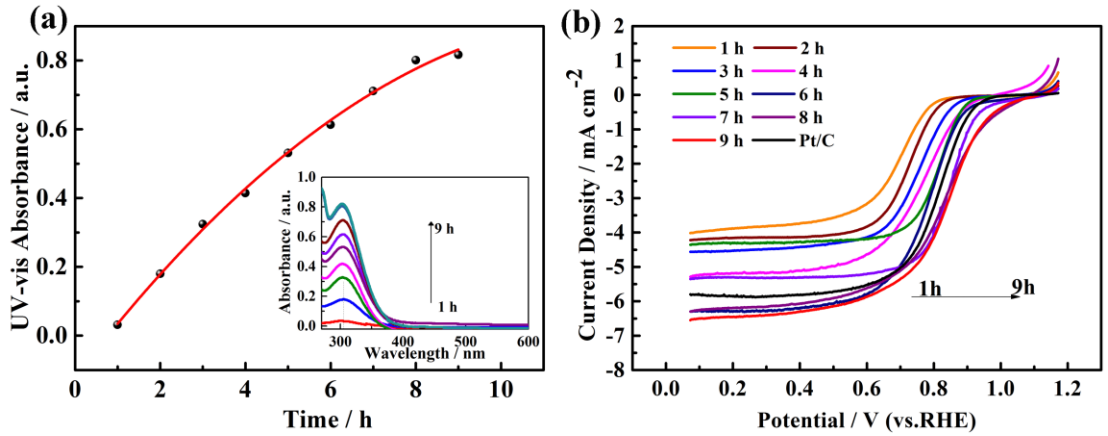

Fig. S9. (a) UV-vis characterization on the Fe-N/C derived from the FeCp@ZIF-8 precursors prepared with different adsorption time. (b) LSV curves (in O_2-saturated 0.1 M KOH solution at 1600 rpm) of Fe-N/C derived from the FeCp@ZIF-8 precursors prepared with different adsorption time.

10. The accelerated durability test of Pt/C.

The accelerated durability test (ADT) of Pt/C was carried out by scanning the CV from 1.00 to 0.60 V at 200 mV s^{-1} in O_2-saturated 0.1 M KOH solution for 10,000 cycles. The LSV of the Pt/C after ADT test shows an obvious negative shift of the potential compared to that before the ADT test (**Fig.** S10). The change of $E_{1/2}$ is about 40 mV, which is larger than that of Fe-N/C-155 (less than 10 mV). This phenomenon illustrates that the as-prepared Fe-N/C-155 in this work has superior stability than the commercial Pt/C.

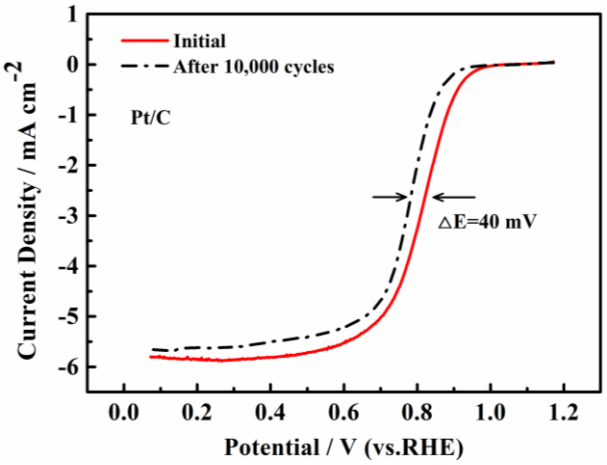

Fig. S10. LSV curves of Pt/C before and after the 10,000 CV cycles.

11. Comparison of different synthetic methods.

To demonstrate the superiority of our cage-confinement synthesis strategy in fabricating Fe-N/C materials, Fe-N/C was also synthesized via classic synthetic methods such as in-situ co-precipitation and impregnation using the same iron source for comparison. The preparation process is as follows.

Synthesis of FeCp-ZIF-8 and FeCp/ZIF-8

For the in-situ co-precipitation approach, 5 mmol of $Zn(NO_3)_2$ $6H_2O$, 80 mg of FeCp and 20 mmol of 2-methylimidazole were dissolved in 100 ml of methanol under vigorous stirring for 4 h and then aged for 24 h at room temperature. The resultant powdery product was collected by filtration, washed with ethanol and DI water, and dried at 60 ℃ overnight. This product was named as FeCp-ZIF-8. For the impregnation strategy, the as-prepared ZIF-8 (200 mg) was dispersed in 30 mL of methanol containing 80 mg of FeCp and stirred for 12 h. The product was named

FeCp/ZIF-8

Synthesis of Fe-N/C-P and Fe-N/C-IP

The as-prepared FeCp-ZIF-8 and FeCp/ZIF-8 were carbonized in a tube furnace under an Ar/H_2 (90/10, v/v) flow. During the high-temperature pyrolysis process, the temperature was firstly raised from room temperature to 200 ℃ at a rate of 5 ℃ min^{-1} and then maintained at 200 ℃ for 2 h. After that, the temperature was further increased from 200 to 800 ℃ at 5 ℃ min^{-1} and kept at 800 ℃ for 2 h. Finally, the pyrolyzed product was treated in a 0.5 M H_2SO_4 solution for 12 h to remove the unstable species, and then collected by filtration, washed with deionized water, and dried overnight at 60 ℃ in an oven. The product derived from FeCp-ZIF-8 and FeCp/ZIF-8 were named as Fe-N/C-P and Fe-N/C-IP, respectively.

UV-vis characterizations of the products prepared by different synthetic methods

Even if twice of the FeCp (mass basis) is added, the UV-vis absorbance strength of either FeCp (250 nm) in the precursor (i.e., FeCp-ZIF-8 and FeCp/ZIF-8) or Fe (305 nm) in Fe, N codoped carbon (i.e., Fe-N/C-P and Fe-N/C-IP) are much less than those in FeCp@ZIF-8 and Fe-N/C-155 (**Fig.** S11), implying the cage-confinement strategy via vapor adsorption is more efficient. The Fe-N/C derived from FeCp@ZIF-8 also shows superior ORR performance than the Fe-N/C-P and Fe-N/C-IP synthesized by the other two methods (**Fig.** S12), demonstrating the superiority of this cage-confinement strategy.

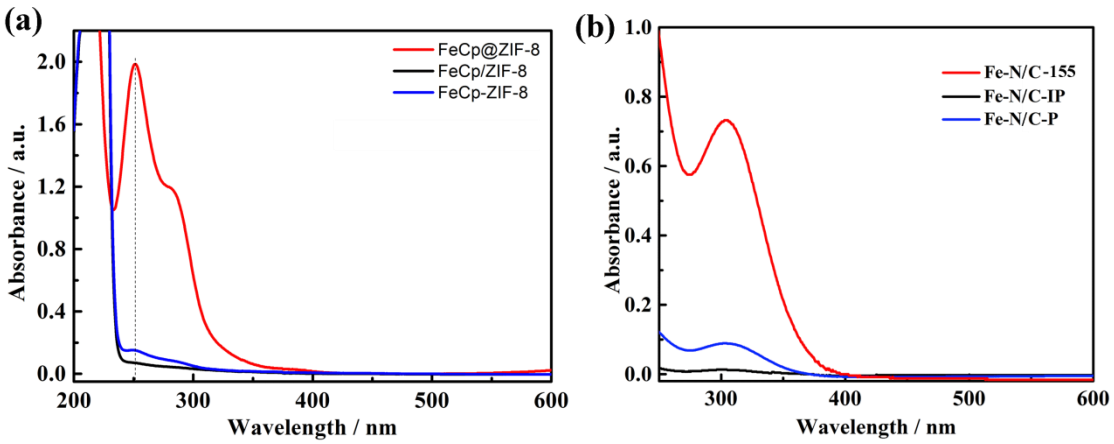

Fig. S11. (a) UV-vis spectra of FeCp@ZIF-8, FeCp-ZIF-8, and FeCp/ZIF-8. (b) UV-vis spectra of Fe-N/C-155, Fe-N/C-P, and Fe-N/C-IP.

Comparison of the ORR performance of Fe-N/C synthesized by different methods

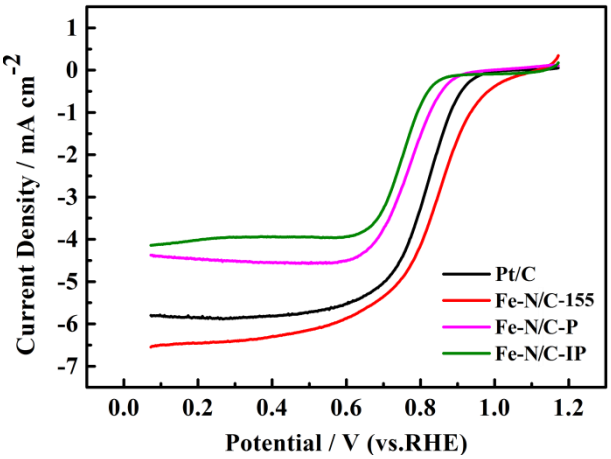

Fig. S12. LSV curves (in O_2-saturated 0.1M KOH solution at 1600 rpm) of Fe-N/C synthesized by different methods.

12. Comparison of the metal loading in the reported single-atom catalysts.

Table S1. Metal loading of single-atom catalysts reported in the literature.

Sample	Metal loading	Application	Reference
Co SAs/N-C	4 wt%	Oxygen Reduction Reaction	Angew. Chem. Int. Ed. 2016 [3]
Fe-N/C	2.9 wt%	Oxygen Reduction Reaction	JACS, 2016 [4]
Co-C_3N_4/CNT	0.2 wt%	Oxygen reduction reaction Oxygen evolution reaction	JACS, 2017 [5]
Fe-N/graphene	1.5 wt%	Catalytic oxidation of benzene to phenol	*Sci. Adv.* **2**015 [6]
Ni SAs/N-C	1.5 wt%	Electro-reduction of Carbon dioxide	JACS, 2017 [7]
Fe_{SA}-N-C	1.76 wt%	Oxygen Reduction Reaction	Angew. Chem. Int. Ed. 2018 [8]
Fe2-Z8-C	3 wt%	Oxygen Reduction Reaction	Angew. Chem. Int. Ed. 2018 [9]
ISAS-Co/HNCS	2.2 wt%	Oxygen Reduction Reaction	JACS, 2017 [10]
Fe-N-CNTAs-5-900	0.09 at%	Oxygen Reduction Reaction	Small 2017 [11]
A-Ni-C	1.5 wt%	Hydrogen Evolution	Nat. Commun. 2016 [12]
Fe-ISAs/CN	2.16 wt%	Oxygen Reduction Reaction	Angew. Chem. Int. Ed. 2018 [13]
FeN4/GN-2.7	2.7 wt%	Oxygen Reduction Reaction	Nano Energy 2017 [14]
Fe-N/C-155	**5.86 wt%**	Oxygen Reduction Reaction	**This work**

13. The overall Fe content in the Fe-N/C samples and their corresponding theoretical content.

The calculation method for the theoretical Fe content is as follows. Assuming no loss of iron atoms during the calcination, the yield of ZIF-8 converted to carbon is about 40% according to the empirical experiment and the TG curve. Then, if the content of Fe in the precursor is *x* wt%, the mass of FeCp and ZIF-8 (in 100 g of FeCp@ZIF-8) are $\left(x \times \frac{186}{56}\right) g$ and $\left(100 - x \times \frac{186}{56}\right) g$, respectively. Assuming all the C and Fe atoms in FeCp are maintained, the calculation formula of the iron content (wt%) in the carbon material obtained after carbonization is $\frac{x}{x \times \frac{176}{56} + \left(100 - x \times \frac{186}{56}\right) \times 40\%} \times 100\%$.

Table S2. The overall Fe content of Fe-N/C based on ICP-OES and calculation

Sample	Fe-N/C-80	Fe-N/C-105	Fe-N/C-130	Fe-N/C-155
ICP-OES / wt%	0.18	1.56	3.20	5.86
Calculation / wt%	0.29	1.55	2.85	5.53

14. The content of C, N and Fe detected by XPS.

Table S3. Element contents in N/C and Fe-N/C determined by XPS

Sample	C at%	N at%	Zn at%	Fe at%	O at%
N/C	82.25	10.24	1.16	——	6.35
Fe-N/C-155	81.13	10.51	0.29	0.86	7.21

15. Estimation of the N content in the Fe-N/C and N/C.

Table S4. Comparison of the N content in Fe-N/C and N/C.

Sample	Content of N (at%)		Reference
	with Fe-doping	without Fe-doping	
Fe-N-CNFs	3.78	9.6 (N-CNFs)	Angew. Chem. 2015 [15]
Fe-ZIF-1100	2.21	2.77 (Fe-free ZIF-1100)	JACS,2017 [16]
5%Fe-N/C	4.49	11.46 (N/C)	ACS Catal. 2017 [1]
Fe−N-DSC	4.5	5.6 (N-DSC)	ACS Nano, 2018 [17]
Fe/N-GPC	3.32	3.59 (N-PC)	ACS Energy Lett. 2017 [18]
Fe-N/C-155	**10.51**	**10.24 (N/C)**	**This work**

16. Estimation of the ORR catalytic performance of the fabricated Fe-N/C-155

Table S5. Comparison of the ORR catalytic performance of the reported Fe-based catalysts in 0.1 M KOH solution.

Catalyst	**Onset potential (V vs. RHE)**	**Half-wave potential (V vs. RHE)**	**Reference**
Fe_{SA}-N-C	——	0.89	Angew. Chem. Int. Ed. 2018 [8]
Fe2-Z8-C	0.985	0.871	Angew. Chem. Int. Ed. 2018 [9]
Fe-N-CNFs	-0.02 (vs. Ag/AgCl)	-0.14 (vs. Ag/AgCl)	Angew. Chem. Int. Ed. 2015 [15]
Fe-N-DSC	1.03	0.84	ACS Nano, 2018 [17]
Fe/N-GPC	-0.01 (vs. Ag/AgCl)	-0.13 (vs. Ag/AgCl)	ACS Energy lett. 2017 [18]
FeN_x-PNC	0.997	0.86	ACS Nano 2018 [19]
Fe@C-NG/NCNTs	0.93	0.84	J. Mater. Chem. A 2017 [20]

pCNT@Fe1.5@GL	0.911	0.811	Adv. Mater. 2017 [21]
$Fe_{0.25}$-N/C-900	——	0.812	Nano Energy 2017 [22]
$Fe/P/C_{0.5}$-800	0.897	0.815	Nano Energy 2017 [23]
Fe-N/C-155	**1.09**	**0.85**	**This work**

Reference

1. Q. Lai, L. Zheng, Y. Liang, J. He, J. Zhao and J. Chen, *ACS Catal*., 2017, **7**, 1655-1663.

2. X. Wang, H. Zhang, H. Lin, S. Gupta, C. Wang, Z. Tao, H. Fu, T. Wang, J. Zheng and G. Wu, *Nano Energy*, 2016, **25**, 110-119.

3. P. Yin, T. Yao, Y. Wu, L. Zheng, Y. Lin, W. Liu, H. Ju, J. Zhu, X. Hong, Z. Deng, G. Zhou, S. Wei and Y. Li, *Angew. Chem., Int. Ed.*, 2016, **55**, 10800-10805.

4. Y. J. Sa, D.-J. Seo, J. Woo, J. T. Lim, J. Y. Cheon, S. Y. Yang, J. M. Lee, D. Kang, T. J. Shin, H. S. Shin, H. Y. Jeong, C. S. Kim, M. G. Kim, T.-Y. Kim and S. H. Joo, *J. Am. Chem. Soc.*, 2016, **138**, 15046-15056.

5. Y. Zheng, Y. Jiao, Y. Zhu, Q. Cai, A. Vasileff, L. H. Li, Y. Han, Y. Chen and S.-Z. Qiao, *J. Am. Chem. Soc.*, 2017, **139**, 3336-3339.

6. D. Deng, X. Chen, L. Yu, X. Wu, Q. Liu, Y. Liu, H. Yang, H. Tian, Y. Hu, P. Du, R. Si, J. Wang, X. Cui, H. Li, J. Xiao, T. Xu, J. Deng, F. Yang, P. N. Duchesne, P. Zhang, J. Zhou, L. Sun, J. Li, X. Pan and X. Bao, *Sci. Adv.*, 2015, **1**, e1500462.

7. C. Zhao, X. Dai, T. Yao, W. Chen, X. Wang, J. Wang, J. Yang, S. Wei, Y. Wu and Y. Li, *J. Am. Chem. Soc.*, 2017, **139**, 8078-8081.

8. L. Jiao, G. Wan, R. Zhang, H. Zhou, S.-H. Yu, H.-L. Jiang, *Angew. Chem. Int. Ed*., 2018, **57**, 1-6.

9. Q. Liu, X. Liu, L. Zheng and J. Shui, *Angew. Chem. Int. Ed.* **2018**, *130*, 1218-1222.

10. Y. Han, Y.-G. Wang, W. Chen, R. Xu, L. Zheng, J. Zhang, J. Luo, R.-A. Shen, Y. Zhu and W.-C. Cheong, *J.Am. Chem. Soc.*, 2017, **139**, 17269-17272.

11. C. Zhu, S. Fu, J. Song, Q. Shi, D. Su, M. H. Engelhard, X .Li, D. Xiao, D. Li and L. Estevez, *Small*, 2017, **13**, 1603407.

12. L. Fan, P. F. Liu, X. Yan, L. Gu, Z. Z. Yang, H. G. Yang, S. Qiu and X. Yao *Nat. Commun*., 2016, **7**, 10667.

13. Y. Chen, S. Ji, Y. Wang, J. Dong, W. Chen, Z. Li, R. Shen, L. Zheng, Z. Zhuang and D. Wang, *Angew. Chem. Int. Ed.*, 2017, **56**, 6937-6941.

14 X. Chen, L. Yu, S. Wang, D. Deng and X. Bao, *Nano Energy*, 2017, **32**, 353-358.

15. Z.-Y. Wu, X.-X. Xu, B.-C. Hu, H.-W. Liang, Y. Lin, L.-F. Chen and S.-H. Yu, *Angew. Chem., Int. Ed.*, 2015, **54**, 8179-8183.

16. H. Zhang, S. Hwang, M. Wang, Z. Feng, S. Karakalos, L. Luo, Z. Qiao, X. Xie, C. Wang, D. Su, Y. Shao and G.Wu, *J. Am. Chem. Soc.*, 2017, **139**, 14143-14149.

17. Z. Huang, H. Pan, W. Yang, H. Zhou, N. Gao, C. Fu, S. Li, H. Li and Y. Kuang, *ACS Nano*, 2018, **12**, 208-216.

18. Q.-L. Zhu, W. Xia, L.-R. Zheng, R. Zou, Z. Liu and Q. Xu, *ACS Energy Lett.*, 2017, **2**, 504-511.

19. L. Ma, S. Chen, Z. Pei, Y. Huang, G. Liang, F. Mo, Q. Yang, J. Su, Y. Gao, J. A. Zapien and C. Zhi, *ACS Nano*, 2018, **12**, 1949-1958.

20. Y. Lei, Q. Wang, Z. Chen, N. Wu, Y. Wang, B. Wang and Y. Wang, *J. Mater. Chem. A*, 2017, **6**, 516-526.

21. S. H. Ahn, X. Yu and A. Manthiram, *Adv. Mater.*, 2017, **29**, 1606534.

22. H. Tan, Y. Li, X. Jiang, J. Tang, Z. Wang, H. Qian, P. Mei, V. Malgras, Y. Bando and Y. Yamauchi, *Nano Energy*, 2017, **36**, 286-294.

23. M. Li, T. Liu, X. Bo, M. Zhou, L. Guo and S. Guo, *Nano Energy*, 2017, **33**, 221-228.